Journal of Colloid and Interface Science 505 (2017) 315–324

Contents lists available at ScienceDirect

Journal of Colloid and Interface Science

journal homepage: www.elsevier.com/locate/jcis

Regular Article

Prediction and control of drop formation modes in microfluidic generation of double emulsions by single-step emulsification

Seyed Ali Nabavi [a,b,1], Goran T. Vladisavljević [a,*], Monalie V. Bandulasena [a], Omid Arjmandi-Tash [a], Vasilije Manović [b,*]

[a] Department of Chemical Engineering, Loughborough University, Loughborough LE11 3TU, United Kingdom
[b] Combustion and CCS Centre, Cranfield University, Cranfield MK43 0AL, United Kingdom

GRAPHICAL ABSTRACT

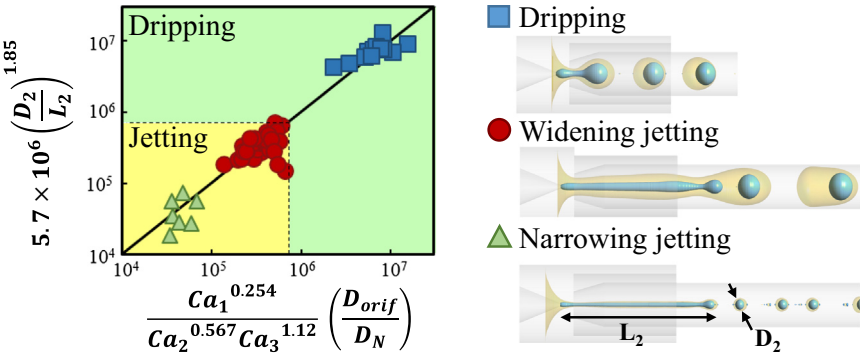

ARTICLE INFO

Article history:
Received 30 April 2017
Revised 28 May 2017
Accepted 30 May 2017
Available online 1 June 2017

Keywords:
Droplet microfluidics
Dripping regime
Narrowing jetting
Widening jetting
Core-shell droplets
Double emulsions
Dripping-to-jetting transition
Velocity profile

ABSTRACT

Hypothesis: Predicting formation mode of double emulsion drops in microfluidic emulsification is crucial for controlling the drop size and morphology.
Experiments and modelling: A three-phase Volume of Fluid-Continuum Surface Force (VOF–CSF) model was developed, validated with analytical solutions, and used to investigate drop formation in different regimes. Experimental investigations were done using a glue-free demountable glass capillary device with a true axisymmetric geometry, capable of readjusting the distance between the two inner capillaries during operation.
Findings: A non-dimensional parameter (ζ) for prediction of double emulsion formation mode as a function of the capillary numbers of all fluids and device geometry was developed and its critical values were determined using simulation and experimental data. At $\log\zeta > 5.7$, drops were formed in dripping mode; the widening jetting occurred at $5 < \log\zeta < 5.7$; while the narrowing jetting was observed at $\log\zeta < 5$. The ζ criterion was correlated with the ratio of the break-up length to drop diameter. The transition from widening to narrowing jetting was achieved by increasing the outer fluid flow rate at the high capillary

Abbreviations: CNC, computer numerical control; CSF, continuum surface force; DC, Dow Corning; I.D., internal diameter; O.D., outer diameter; OTMS, octadecyltrimethoxysilane; PDMS, polydimethylsiloxane; PVA, polyvinyl alcohol; VOF, volume of fluid.

* Corresponding authors.
E-mail addresses: g.vladisavljevic@lboro.ac.uk (G.T. Vladisavljević), v.manovic@cranfield.ac.uk (V. Manović).
[1] Present address: Combustion and CCS Centre, Cranfield University, Cranfield MK43 0AL, United Kingdom.

http://dx.doi.org/10.1016/j.jcis.2017.05.115
0021-9797/

Nomenclature

C'	constant, –
Ca	capillary number, –
D	diameter, m
D_1	inner droplet diameter, m
D_2	outer droplet diameter, m
f	drop generation frequency, s^{-1}
f'	volume fraction, –
F_b	body force, N m^{-3}
F_σ	interfacial force, N m^{-3}
L	break-up length, m
in	maximum instability, –
$\hat{n}$	unit normal, –
P	pressure, Pa
Q	volume flow rate, m^3 s^{-1}
r	radial distance, m
r_c	radius of collection capillary, m
t	time, s
V	velocity, m s^{-1}
X	axial distance, m
x	direction (coordinates), m
α	diameter ratio, –
κ	curvature of interface, m^{-1}
μ	dynamic viscosity, kg·(m s)$^{-1}$
ρ	density, kg m^{-3}
σ	interfacial tension, N m^{-1}

Subscripts

1	inner phase
2	middle phase
3	outer phase
1,2	between inner and middle phase
2,3	between middle and outer phase
c	capillary
ci	injection capillary
co	outer capillary
continuous	continuous phase
dispersed	dispersed phase
ef	effective
j	jet
N	injection nozzle
orif	orifice

Volume of fluid–continuum surface force model
Glass capillary device

number of the inner fluid. The drop size was reduced by reducing the distance between the two inner capillaries and the minimum drop size was achieved when the distance between the capillaries was zero.

1. Introduction

Core-shell capsules attract great interest for potential applications ranging from controlled release of drugs and nutrients [1–4], encapsulation of fragrances [5], to CO_2 capture and energy storage [6–8]. The conventional fabrication strategies for core-shell capsules such as complex coacervation [9], internal phase separation [10], layer-by-layer electrostatic deposition [11], interfacial polymerisation [12], and spray drying [13] often require multistage processing and are associated with low encapsulation efficiency, low reproducibility and a lack of control over the size of the capsules and the shell thickness. In addition, the synthesised particles are usually highly polydispersed [14].

Microfluidic emulsification is a promising strategy for production of monodispersed double emulsions with controlled drop size and morphology. Double emulsion drops can be created through single-step or two-step emulsification methods, using flow-focusing [15,16], cross-flow [17,18] or co-flow [19,20] drop makers. Utada et al. [21] developed a three-phase 3D glass capillary device for single-step generation of double emulsions by combining co-flow and counter-current flow focusing flow patterns. The device consists of two tapered round capillaries, coaxially aligned within a square capillary and separated at some distance from each other, Fig. 1a and b. The device provides precise control over the droplet size and shell thickness. The wettability of each capillary can be independently modified, which is advantageous compared to polydimethylsiloxane (PDMS) devices that suffer from poor wettability control [22]. However, the distance between the round capillaries is fixed during operation and the device is difficult to clean after use.

The drop formation in capillary devices occurs in two distinct instability modes, absolute and convective [23]. Dripping is the result of an absolute instability; the perturbations that lead to drop pinch-off grow at a fixed spatial location and at a frequency that is intrinsic to the system, leading to monodispersed drops. Jetting occurs due to convective instability, which is associated with the advection of the perturbations along the interface of the jet, which causes random variation in the pinch-off location. Therefore, the drops generated in jetting mode are polydispersed [23,24]. The mechanism of drop formation in each mode is governed by the interaction between viscous, inertial, interfacial, and gravitational forces [25]. However, the effect of gravity is negligible when the drop diameter is in the micrometre range [26,27].

In dripping mode, the interfacial force is dominant and the inertial forces are negligible. The drops are formed in the vicinity of the injection nozzle (in co-flow geometry) or within one orifice diameter downstream of the orifice of the collection capillary (in flow-focusing geometry) once the viscous force, exerted by the continuous phase, exceeds the pinning force arising from the interfacial tension [27,29].

Two types of jetting mode have been observed in capillary devices, narrowing and widening [30]. Narrowing jetting is associated with formation of a relatively thin and long jet that eventually breaks into small drops; this mode occurs when the viscous force generated by the continuous phase is significantly greater than the interfacial force. On the other hand, widening jetting occurs when the inertial forces of the jet dominate the interfacial tension force. The widening shape of the jet has been attributed to the deceleration of the jet [31].

The formation of single emulsion drops in two-phase glass capillary devices is well characterised [27,30–33]. In three-phase glass capillary devices, inner and outer drops can be formed in the same or different modes and thus, versatile drop morphologies can be achieved. Due to complexity of the coaxial jet

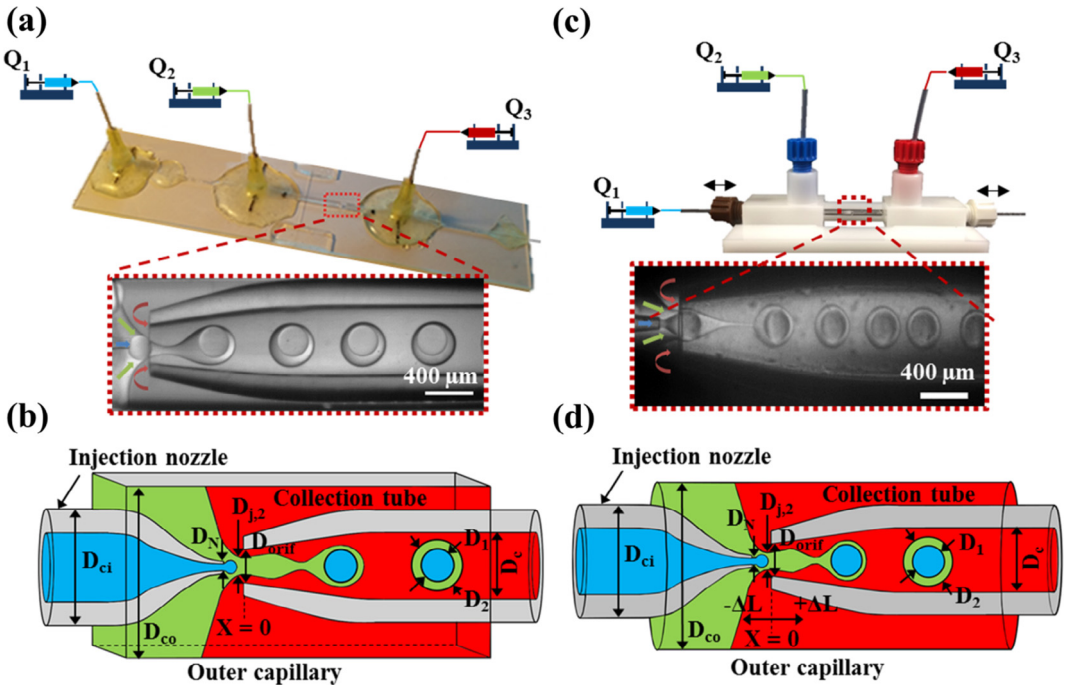

Fig. 1. Glass capillary devices used in this study along with corresponding micrographs of double emulsion formation: (a) A photograph and (b) scheme of the standard device with a square outer capillary attached onto the microscope slide; (c) A photograph and (d) scheme of a glue-free device with a round outer capillary and a milled polyacetal holder. Supplementary movie S1.

pinch-off, only a few studies have been carried out on the double emulsion formation in three-phase capillary devices and the prediction of drop sizes in dripping and jetting modes [21,29,34,35]. Utada et al. [21] studied the formation of core-shell drops in both dripping and widening jetting modes and found that double emulsions were not formed when the outer drops were formed in dripping mode and the inner drops in jetting mode. Although double emulsion formation by narrowing jetting has been reproduced numerically [29,35], it has not yet been observed experimentally in glass capillary devices. In addition, the variation of the distance between the inner capillaries changed the drop formation mode in numerical simulations [29], but no experimental evidence has been provided so far. Lee and Weitz [34] observed the formation of multi-core double-emulsion drops in capillary devices in an inertia-induced dripping-to-widening jetting transition mode at relatively high flow rates of the inner and middle fluids. To the best of our knowledge, no parameter capable of predicting the drop formation regime in capillary microfluidics has been developed so far.

In this study, a novel dimensionless criterion, $\log\zeta$, that can be used for prediction of drop formation mode in three-phase glass capillary devices, was introduced and its critical values at which transitions occur were determined using a large amount of simulation and experimental data. Different transitions of drop formation modes were observed experimentally and a high ability of $\log\zeta$ to accurately predict the drop formation behaviour was confirmed. In addition, a glue-free, detachable and reusable three-phase glass capillary device was fabricated, with the ability to adjust the distance between the opposing inner capillaries during operation. The device consists only of round capillaries and has a true axisymmetric geometry, unlike conventional capillary devices consisting of round inner capillaries placed within a square outer capillary, which have a quasi-axisymmetric geometry. The device was used to reveal the significant impact of the distance between the two tapered inner capillaries on droplet formation behaviour.

2. Materials and methods

2.1. Governing equations and numerical method

2.1.1. Governing equations

A two-dimensional incompressible axisymmetric Volume of Fluid-Continuum Surface Force (VOF-CSF) [36,37] numerical model has been developed to simulate double emulsion formation. The governing mass, Eq. (1), and momentum, Eq. (2), balance equations are:

$$\frac{\partial\rho}{\partial t}+\frac{\partial(\rho V_i)}{\partial x_i}=0 \tag{1}$$

$$\frac{\partial(\rho V_i)}{\partial t}+\frac{\partial(\rho V_i V_j)}{\partial x_j}=-\frac{\partial P_i}{\partial x_i}+\frac{\partial}{\partial x_j}\left(\mu\frac{\partial V_i}{\partial x_j}\right)+F_b \tag{2}$$

where V and P are the velocity and pressure, respectively, while t, μ, and ρ are the time, dynamic viscosity and density. F_b is a source term which includes interfacial force, F_σ and gravitational force. Since the drop diameter is in the order of micrometres, the gravitational force is negligible and $F_b = F_\sigma$ [26,27]. In the VOF method, a momentum balance equation is solved for all the phases and the advection of interface is calculated by solving a transport equation, Eq. (3), for volume fraction, f':

$$\frac{\partial f'}{\partial t}+\frac{\partial(V_i f')}{\partial x_i}=0 \tag{3}$$

The volume fraction gives the portion of the cell which is filled with either phase, where

$$\begin{aligned} &f'=0 \quad \text{the cell is filled with dispersed phase fluid}\\ &0<f'<1 \quad \text{the interface exists in the cell}\\ &f'=1 \quad \text{the cell is filled with continuous fluid} \end{aligned} \tag{4}$$

The μ and values in Eq. (2), were calculated using Eqs. (5) and (6), respectively:

$$\mu = f'\mu_{continuous} + (1 - f')\mu_{dispersed} \quad (5)$$

$$\rho = f'\rho_{continuous} + (1 - f')\rho_{dispersed} \quad (6)$$

The CSF method was used to calculate F_b in Eq. (2) at the interface:

$$F_b = \sigma\kappa\nabla f' \quad (7)$$

where σ is the interfacial tension and κ is the local curvature of the interface, given by:

$$\kappa = \nabla \cdot \hat{n} \quad (8)$$

and $\hat{n}$ is the unit normal, given by Eq. (9):

$$\hat{n} = \frac{\nabla f'}{|\nabla f'|} \quad (9)$$

2.1.2. Numerical method

An unsteady-flow pressure-based segregated algorithm, established in finite-volume-based commercial software Ansys® Fluent v. 14.0, was used to solve the governing equations. The discretised moment equation was approximated using a second order upwind scheme. The PRESTO scheme was used to interpolate the pressure term. Although the PRESTO scheme is computationally expensive, it directly calculates the pressures at cell faces and avoids interpolation errors. The pressure and velocity were coupled using the SIMPLE scheme. The interface interpolation was obtained by the Geo-Reconstruct algorithm. A variable-time-step method based on the maximum Courant number of 0.35 was used to reduce the computational cost. To evaluate grid independence, five meshes with a resolution of 8 μm, 4 μm, 3 μm, 2 μm, and 1 μm were constructed. The difference in simulation results obtained with the resolutions of 1, 2, and 4 μm was negligible. Therefore, a mesh size of 2 μm was used around the injection orifice and inside the collection tube where the drops were formed, while a coarser mesh was used for the rest of the domain. Further details on the numerical model can be found elsewhere [29,38].

2.1.3. Dimensionless numbers

Non-dimensional numbers used in this study are the capillary numbers of inner, Ca_1, middle, Ca_2, and outer phase, Ca_3, given by:

$$Ca_1 = \frac{\mu_1 V_1}{\sigma_{12}} \quad Ca_2 = \frac{\mu_2 V_2}{\sigma_{23}} \quad Ca_3 = \frac{\mu_3 V_3}{\sigma_{23}}$$

where $V_1 = 4Q_1/(\pi D_N^2)$, $V_2 = Q_2/(D_{co}^2 - \pi D_{ci}^2/4)$, $V_3 = Q_3/(D_{co}^2 - \pi D_{ci}^2/4)$. Subscripts 1, 2 and 3 stand for the inner, middle and outer phase, respectively, D_{ci} is the outer diameter of the injection capillary, and D_{co} is the internal height of the square capillary, Fig. 1b.

2.2. Materials

Glycerol was supplied by Fisher Scientific (UK) and used as a viscosity modifier. Polyvinyl alcohol (PVA, M_w = 13,000–23,000 g mol^{-1}, 87–89% hydrolysed) was purchased from Sigma-Aldrich (UK) and used as a hydrophilic stabiliser. Dow Corning® 749 Fluid (DC 749) was supplied by Univar (UK) and used as a lipophilic surfactant. Polydimethyl siloxane (PDMS) fluid (Dow Corning 200/10cs fluid) was obtained from VWR (UK) and used as the main constituent in the middle phase. 2-[methoxy(polyethyleneoxy)propyl]trimethoxysilane and octadecyltrimethoxysilane (OTMS) were purchased from Fluorochem, Ltd. (UK) and used for hydrophilic and hydrophobic treatment of glass capillaries. The Millipore Milli-Q Plus water purification system was used to produce water for preparing all aqueous solutions. The density, dynamic viscosity and interfacial tension were measured using pycnometer, capillary viscometer, and Krüss DSA-100 pendant drop tensiometer, respectively.

2.3. Droplet production

Fabrication of microfluidic devices: Two different kinds of three-phase glass capillary device were used in this study: standard and novel. In a standard device, inner capillaries were manually centred within a square capillary and fixed on a microscope slide using a two-part epoxy (Devcon 5-Minute Epoxy®) [29,38]. In this device, the capillaries are fixed in place and the distance between inner capillaries cannot be changed. This fabrication process is tedious and the device is difficult to clean; after several experiments, when the capillaries become fouled, a new device must be made. Hence, a novel glue-free separable device was designed and manufactured. The device has an adjustable distance between inner capillaries, which can be changed during operation and can be dismantled, cleaned and reassembled. The device is easier to fabricate since all the capillaries are placed into an engineered holder to avoid the manual centring. The holder was made of acetal copolymer with a density of 1.41 g/cm^3, and manufactured by Computer Numerical Control (CNC) machining using a fully automated HAAS Super Mini Mill machine (HAAS Automation, Norwich, UK), Fig. 1c. The holder is similar to the 3D-printed holder developed by Martino et al. [39], but CNC milling offers a wide range of materials for manufacturing and provides a superior surface quality. First, round borosilicate glass capillaries of 1/0.58 mm (O.D./I.D.) (Intracel, UK) were pulled using a Flaming/Brown micropipette puller (P-97, Sutter Instrument Co., Linton Instrumentation, Norfolk, UK) to obtain injection and collection capillary tubes. The pulled capillaries were polished to the desired tip size using an abrasive paper (Black Ice Waterproof T402 Paper, Alpine Abrasives, UK) under visual control with the aid of a Narishige Model MF-830 microforge (Japan). A borosilicate round capillary of 2/1.56 mm (O.D/I.D.) (World Precision Instruments, UK) was then placed in the holder and used as the outer capillary. Then, the injection and collection capillaries were inserted into the outer capillary at both ends. Finally, Omnifit connectors were attached to the holder and used for introduction of the three fluids into the device, Fig. 1c.

Double emulsion formation: Three gas-tight glass syringes with Luer-lock fitting (VWR Catalyst Company, UK) were filled with the three fluids and placed on Harvard Apparatus 11 Elite syringe pumps. The inner phase was 5–85 wt% aqueous glycerol solution, the middle phase was 2 wt% DC 749 in PDMS fluid, and the outer phase was an aqueous solution containing 40–70 wt% glycerol and 2 wt% PVA. The fluids were delivered into the device using polyethylene medical tubing of 1.52/0.86 mm (O.D./I.D.) (Fisher Scientific, UK). Double emulsion drops were formed upon breakup of the coaxial jet composed of inner and middle fluids in the collection tube, Fig. 1b. The drop generation was monitored and recorded using Phantom V9.0 high-speed camera (Vision Research, UK) attached to an inverted microscope (XDS-3, GX Microscopes, UK) and interfaced to a PC computer. The ImageJ program developed at the National Institute of Health was used to analyse the captured frames.

3. Results and discussion

3.1. Validation of numerical model

The developed numerical model was validated with several analytical models in terms of the inner and outer drop sizes, D_1 and D_2, respectively. In the dripping mode, the numerical D_2 values were validated using analytical models developed by Erb et al. [28]

and Utada et al. [21]. Erb et al.'s analytical model is given by Eq. (10) [28]:

$$D_2^4 + \Gamma(Q_3 + Q^*)D_2^3 - [D_{orif,ef}^2 + \Gamma D_{j,2}(Q_3 + Q^*)]D_2^2 - \Gamma Q^* D_{orif,ef}^2 D_2 + \Gamma Q^* D_{orif,ef}^2 D_{j,2} = 0 \quad (10)$$

where

$$\Gamma = 120\mu_3/[\pi(D_{j,2}\sigma_{23} + D_{j,1}\sigma_{12})]$$

$$D_{j,2} = D_{orif}\sqrt{(Q_1 + Q_2)/(Q_1 + Q_2 + Q_3)}$$

$$D_{j,1} = D_{j,2}\sqrt{Q_1/(Q_1 + Q_2)}$$

$$Q^* = Q_2/\left[1 - (Q_1/(Q_1 + Q_2))^{2/3}\right]$$

$D_{j,2}$ and $D_{j,1}$ are the diameter of outer and inner jets at the orifice of the collection capillary, and $D_{orif,ef}$ is the effective orifice diameter, which corresponds to the diameter of the collection tube at the location where the double emulsion drops are pinched off. The model developed by Utada et al. [21] for dripping mode is given by the equation:

$$D_2 = kD_{j,2} \quad (11)$$

where $k = (3\pi/2in)^{1/3}$ and $D_{j,2}$ can be calculated using Eq. (12):

$$\frac{Q_1 + Q_2}{Q_3} = \frac{D_{j,2}^2}{D_{orif}^2 - D_{j,2}^2} \quad (12)$$

The proportionality constant k in Eq. (11) depends on the maximum instability (in), which is a function of the viscosity ratio, $\mu_{dispersed}/\mu_3$ [40,41], where $\mu_{dispersed}$ is the effective viscosity of the mixture of inner and middle phases. In current simulations, since the shell was relatively thick and the middle phase was much more viscous than the inner phase ($\mu_2 \gg \mu_1$), $\mu_{dispersed}$ was approximated with the viscosity of pure middle phase, μ_2 and in = 0.55. In jetting mode, D_2 can be predicted using Eq. (13) developed by Utada et al. [21]:

$$D_2 = \left(\frac{3C'(Q_1 + Q_2)}{8\pi}\frac{D_{j,2}\mu_3}{\sigma_{23}}\right)^{1/3} \quad (13)$$

where C' is a constant, which depends on the viscosity ratio, μ_2/μ_3 [42]. In this work, C' = 79.4 and $D_{j,2}$ can be estimated by solving Eq. (14) for α ($\alpha = D_{j,2}/D_{orif}$) [21]:

$$\frac{Q_1 + Q_2}{Q_3} = \frac{\mu_3}{\mu_2}\frac{\alpha^4}{(1 - \alpha^2)^2} + 2\frac{\alpha^2}{1 - \alpha^2} \quad (14)$$

For both regimes, D_1 can be calculated from D_2 using the mass balance equation:

$$\frac{D_2}{D_1} = \left(\frac{Q_1 + Q_2}{Q_1}\right)^{1/3} \quad (15)$$

Fig. 2 shows the validation of the present numerical model with existing analytical models in both dripping (green region) and jetting (yellow region) regimes. A very good agreement between the numerical and analytical results was achieved in both regimes, implying the high accuracy of the developed numerical model in predicting flow behaviour in the device. The slight discrepancy between the numerical result and Erb et al.'s model in the dripping regime at $Q_3/(Q_1 + Q_2)$ = 1.44 can be attributed to the variation of $D_{orif,ef}$ with Q_3, because the break-up length is a function of Q_3. However, an average $D_{orif,ef}$ value of 408 μm ($1.36D_{orif}$) was used for the validation. The available analytical models are valid only in dripping or jetting regime. No existing analytical model can predict the drop size in the dripping-to-jetting transitional regime, at $Q_1/(Q_2 + Q_3)$ between 5 and 12 (the blue region in Fig. 2).

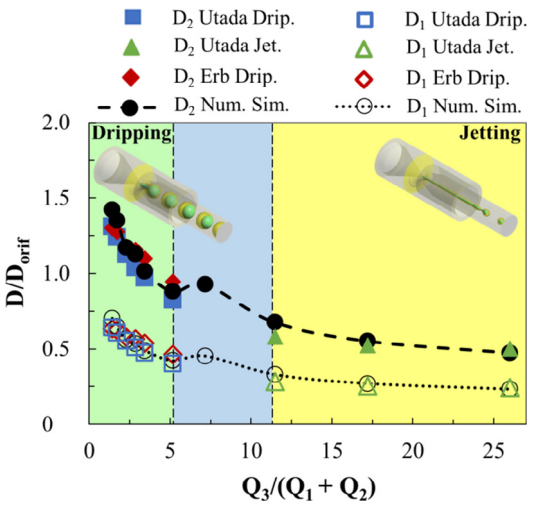

Fig. 2. Validation of the developed numerical model with existing analytical models. Q_1 = 0.12 mL/h, Q_2 = 0.92 mL/h, ρ_1 = 1180 kg/m^3, ρ_2 = 1170 kg/m^3, ρ_3 = 1200 kg/m^3, μ_1 = 39.6 mPa s, μ_2 = 64.8 mPa s, μ_3 = 48.2 mPa s, σ_{12} = 5.7 mN/m, σ_{23} = 13.7 mN/m, D_{orif} = 300 μm. Green, blue, and yellow background colours represent dripping, dripping-to-jetting transitional, and jetting regions, respectively. (For interpretation of the references to colour in this figure legend, the reader is referred to the web version of this article.)

3.2. Evolution of velocity profile in collection tube in different drop formation modes

Fig. 3 shows the evolution of cross-sectional normalised stream-wise velocity profiles along the collection tube in different drop formation modes. Starting from the dripping mode, Fig. 3a, the widening jetting was obtained by increasing Q_2 from 0.92 to 2.47 mL/h, Fig. 3b, and the narrowing jetting was achieved by increasing Q_3 from 2.47 to 24 mL/h, Fig. 3c, while keeping all other parameters constant. In each graph the two red diamonds indicate the locations of the inner and outer interface. At the entrance of the collection tube (X = 0), the velocity profiles in dripping and widening jetting are flat and equal to the centreline velocity (V at r = 0), except within the boundary layer where the velocity decreases sharply to zero at the tube wall. The centreline velocity in the widening jetting mode was larger than in the dripping mode, due to higher Q_2. At X = 0, a saddle-shaped velocity profile was observed in the narrowing jetting regime and the maximum velocity was observed in the continuous phase stream at r/r_c = 0.26. Due to the strong elongational flow of the outermost fluid that pulls the jet downstream, the centreline velocity was much larger in the narrowing jetting than in the widening jetting and dripping modes, although Q_1 was the same. The two red diamonds almost overlap each other due to small shell thickness and both interfaces are very close to the centreline due to jet thinning by strong shear and pressure forces.

In the dripping regime, the velocity profile further downstream remained almost flat, Fig. 3a, but at $X = 1.13D_{orif}$ the velocity of the outermost fluid was higher than the velocity of the middle and inner fluids, due to jet widening at the tip as a result of drop formation. The centreline velocity decreases along the tube due to an increase in the tube cross-sectional area. In the widening jetting mode, the velocity profiles further downstream approach a parabolic shape with the maximum velocity located at the centreline. The velocity at the tube axis increases at $X = 4.58D_{orif}$ due to necking of the inner jet. In the narrowing jetting regime, the velocity

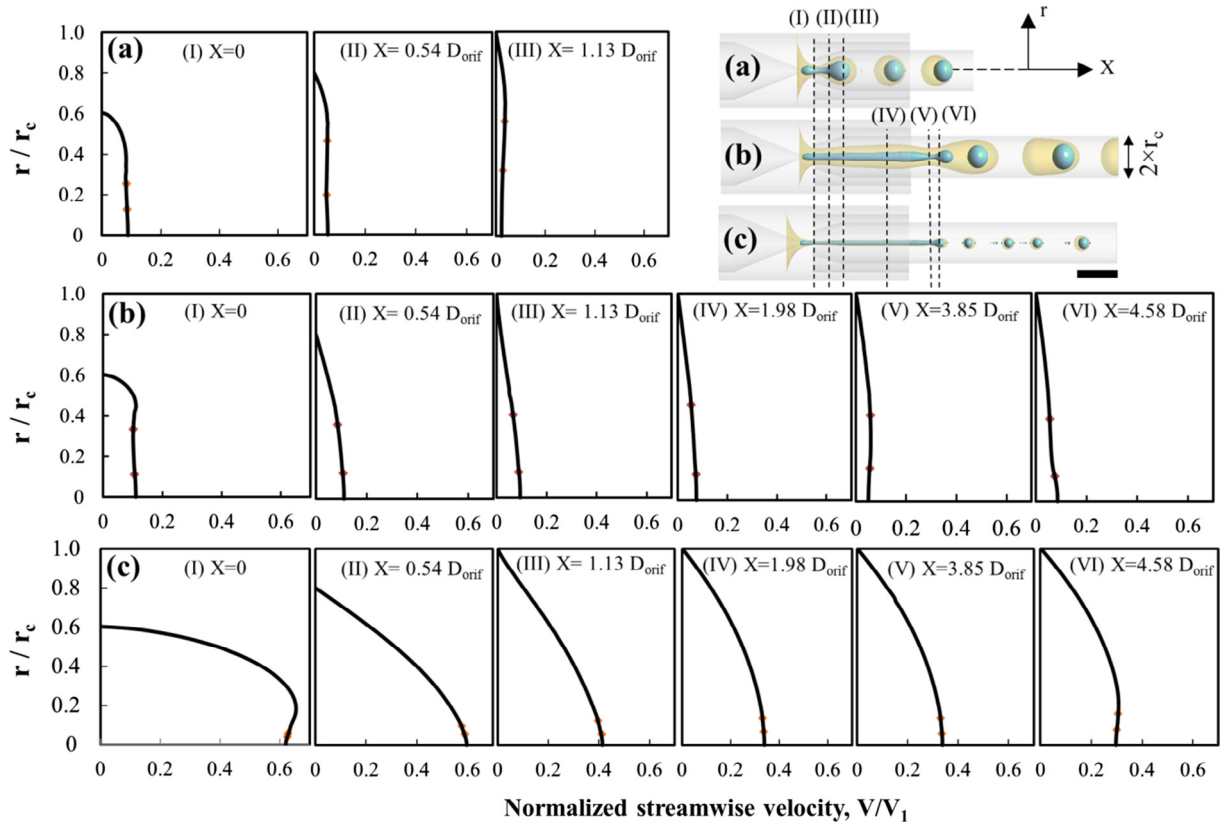

Fig. 3. The velocity profiles across the collection capillary tube determined by numerical simulations: (a) Dripping regime at Q_1 = 0.37 mL/h, Q_2 = 0.92 mL/h, Q_3 = 2.47 mL/h; (b) Widening jetting regime at Q_1 = 0.37 mL/h, Q_2 = 2.31 mL/h, Q_3 = 2.47 mL/h; (c) Narrowing jetting regime at Q_1 = 0.37 mL/h, Q_2 = 0.92 mL/h, Q_3 = 24 mL/h. The constants: ρ_1 = 1180 kg/m^3, ρ_2 = 1170 kg/m^3, ρ_3 = 1200 kg/m^3, μ_1 = 39.6 mPa s, μ_2 = 64.8 mPa s, μ_3 = 48.2 mPa s, σ_{12} = 5.7 mN/m, σ_{23} = 13.7 mN/m, V_1 = 0.2 m/s, D_{orif} = 300 μm. The inner radius of the collection tube downstream of the tapered section is r_c = 250 μm and the length of the tapered section is $1.13D_{orif}$. The scale bar is 500 μm.

profile changes from a saddle shape at $X = 0$ to parabolic at $X = 3.85D_{orif}$. In addition, almost the same velocity profile with a small decrease in the centreline velocity was observed until the end of the computational domain.

3.3. Prediction of double emulsion formation mode

Each drop generation mode can be characterised with a certain range of D_2/L_2 values, where L_2 is the break-up length, i.e., the distance from the orifice of the injection capillary to the point of drop pinch-off. In dripping mode, D_2 is similar to D_{orif}, while L_2 is very small, thus D_2/L_2 is relatively large ($D_2/L_2 > 0.3$). In narrowing jetting mode, D_2 is small and L_2 is large and consequently, D_2/L_2 is small ($D_2/L_2 < 0.1$). In widening jetting, D_2 is larger than in narrowing jetting and dripping mode, but L_2 is much larger than in dripping mode and thus, D_2/L_2 is between the limits for the dripping and narrowing jetting mode ($0.1 < D_2/L_2 < 0.3$). The drop formation mode can be altered by changing fluid properties and flow rates [29], which can be expressed in terms of Ca_1, Ca_2, and Ca_3. Moreover, the variations in D_{orif} can impact the drop formation regime with higher D_{orif} values favouring the dripping mode [29]. The numerical results collected over a wide range of fluid properties, flow rates and device geometries were analysed to develop an empirical parameter, ζ, that can be used for prediction of the double emulsion formation regime:

$$\zeta = \left[\frac{Ca_1^{0.254}}{Ca_2^{0.567}Ca_3^{1.12}}\right]\left[\frac{D_{orif}}{D_N}\right] \quad (16)$$

where ζ can be calculated from Eq. (16) or measured from D_2/L_2 using the equation: $\zeta_{measured} = 5.7 \times 10^6 (D_2/L_2)^{1.85}$. The comparison of ζ values calculated from Eq. (16) and measured from the numerical D_2/L_2 values is shown in Fig. 4.

Good agreement between the measured and calculated ζ values was achieved. For $\log\zeta > 5.7$ (green region), double emulsion was formed in dripping mode, while $\log\zeta < 5.7$ (yellow region) was

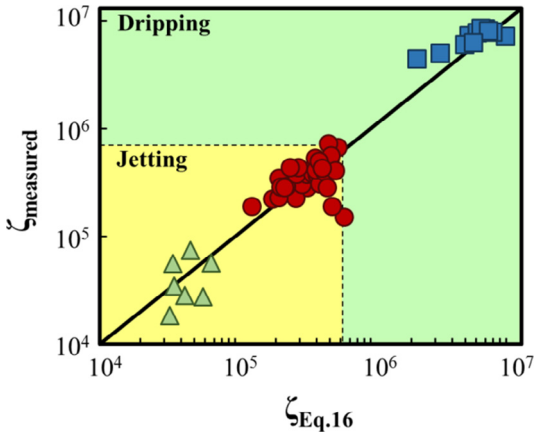

Fig. 4. Comparison of $\zeta_{measured}$ and $\zeta_{Eq.\ 16}$ in numerical simulations. The diagonal line shows the perfect match: $\zeta_{measured} = \zeta_{Eq.\ 16}$. The operating conditions: Q_1 = 1–1.5 mL/h, Q_2 = 0.9–3.4 mL/h, Q_3 = 1.5–15 mL/h, μ_1 = 7–95 mPa s, μ_2 = 8–75 mPa s, μ_3 = 24–80 mPa s, σ_{12} = 5.7 mN/m, σ_{23} = 13.7–41 mN/m, D_{orif}/D_N = 6–12, D_N = 26 μm. The drop formation regime: Dripping ■; Widening jetting ●; Narrowing jetting ▲.

associated with the jetting mode. The widening jetting regime was observed for $5 < \log\zeta < 5.7$, while the narrowing jetting mode occurred at $\log\zeta < 5$. The transition between the regimes was not sharp but occurred gradually near the critical $\log\zeta$ values, which might cause inaccurate regime predictions near the critical ζ values. The ability of $\log\zeta$ to predict the drop formation regime was tested experimentally in Figs. 5 and 6. In most cases, $\log\zeta$ calculated from Eq. (16) was able to accurately predict the drop formation regime. In addition, $\log\zeta$ was calculated for the numerical data points in Fig. 2 and the results are shown in Fig. S1 in the supplementary material. The dripping-to-jetting transition occurred at $\log\zeta = 5.7$. The D_2/L_2 values were plotted on the same graph and

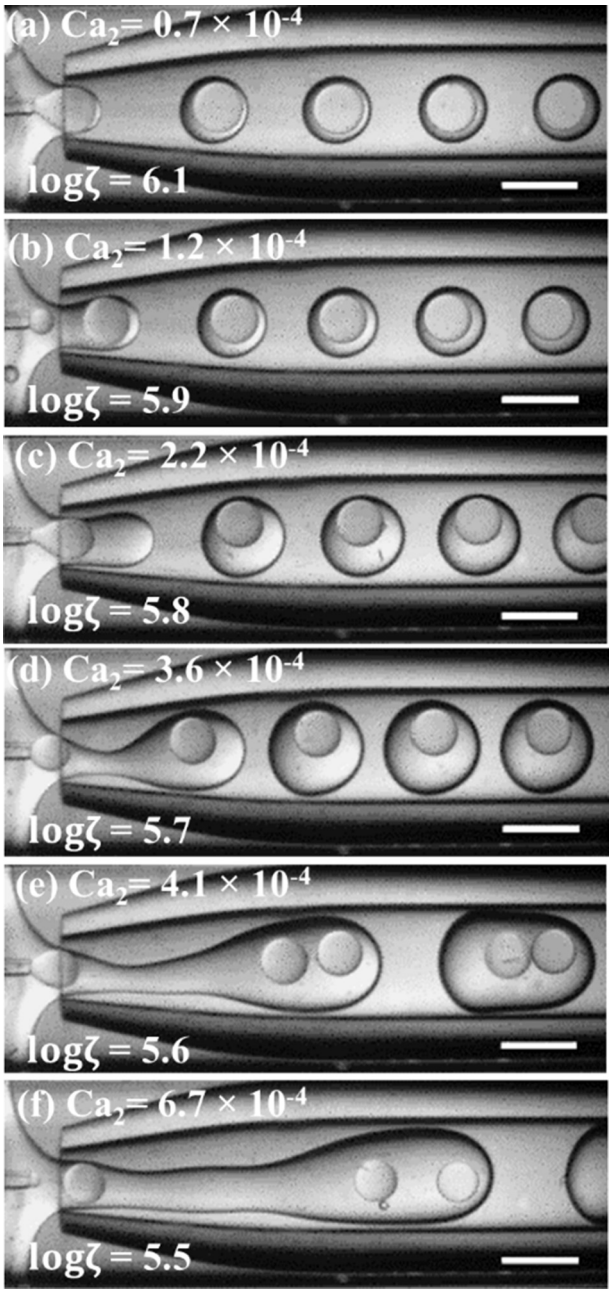

Fig. 5. The dripping-to-widening jetting transformation achieved by increasing Ca_2 at: $Ca_1 = 0.1$, $Ca_3 = 1.5 \times 10^{-3}$, $\rho_1 = 1225$ kg/m^3, $\rho_2 = 940$ kg/m^3, $\rho_3 = 1118$ kg/m^3, $\mu_1 = 109$ mPa s, $\mu_2 = 10.4$ mPa s, $\mu_3 = 33$ mPa s, $\sigma_{12} = 29.9$ mN/m, $\sigma_{23} = 31.8$ mN/m, $D_{orif} = 327$ μm, and $D_N = 50$ μm. Logζ was calculated using Eq. (16). The scale bars are 400 μm.

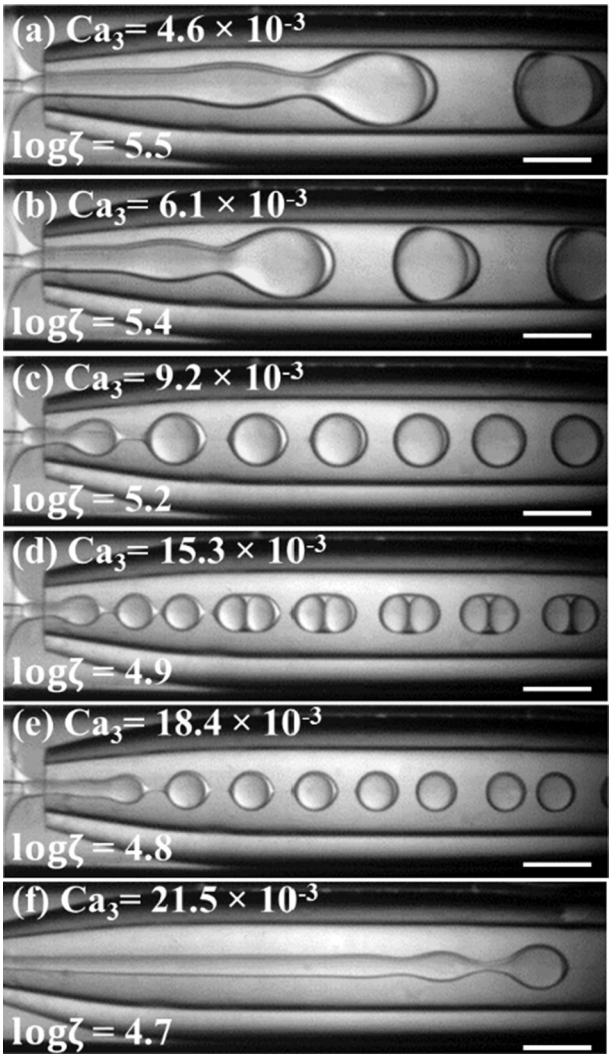

Fig. 6. The widening-jetting-to-narrowing-jetting transition achieved by increasing Ca_3 at: $Ca_1 = 1.3$, $Ca_2 = 2.4 \times 10^{-4}$, $\rho_1 = 1225$ kg/m^3, $\rho_2 = 940$ kg/m^3, $\rho_3 = 1118$ kg/m^3, $\mu_1 = 109$ mPa s, $\mu_2 = 10.4$ mPa s, $\mu_3 = 33$ mPa s, $\sigma_{12} = 29.9$ mN/m, $\sigma_{23} = 31.8$ mN/m, $D_{orif} = 327$ μm and $D_N = 50$ μm. Logζ was calculated using Eq. (16). The scale bars are 500 μm.

the dripping-to-jetting transition occurred at D_2/L_2=0.3, as predicted. It should be highlighted that Eq. (16) was developed for primary drops and does not take into account the formation of satellite drops.

3.4. Transitions of drop generation modes

In this section, the effect of Ca_1, Ca_2, and Ca_3 on the transitions of drop generation regimes has been investigated experimentally. The inner phase was 85 wt% aqueous solution of glycerol. The middle phase consisted of 2 wt% DC 749 in PDMS fluid, and the outer phase was a mixture of 70 wt% glycerol and 2 wt% PVA in water. Core-shell drops produced using this formulation were stable for at least several hours after production [8,43]. Fig. 5 shows the transition from the dripping to widening jetting achieved by increasing Q_2 and thereby Ca_2 at constant values of Ca_3 and Ca_1. An increase in Ca_2 from 0.7×10^{-4} to 3.6×10^{-4} (Fig. 5a–d) caused an increase in D_2 from 361 to 504 μm and a decrease in D_1 from 266 to 245 μm, which resulted in 2.7 times thicker shell. The reduction in D_1 was due to higher shear force exerted by the middle phase on the inner liquid, which led to faster

generation of inner drops. According to the mass balance equation: $Q_1 = f_1 \pi D_1^3/6$, higher drop generation frequency, f_1, at Q_1 = constant results in smaller D_1. An increase in D_2 can be attributed to the larger inertia of the middle phase at higher Ca_2 and introduction of a higher amount of the middle phase into the outer drop prior to drop pinch-off [29].

In Fig. 5a–c, the outer drops were formed in dripping mode ($\log\zeta > 5.7$), but in Fig. 5d, the value of $\log\zeta$ was at the boundary between dripping and widening jetting. At $Ca_2 = 4.1 \times 10^{-4}$ (Fig. 5e), the outer drops were formed in the widening jetting regime ($\log\zeta = 5.6$); two smaller inner drops were encapsulated within each outer drop and the diameter of the outer drops was larger than the diameter of the collection tube. At $Ca_2 = 6.7 \times 10^{-4}$ (Fig. 5f), the outer drops were formed by pinching of a long, wide jet ($D_2/L_2 < 0.3$), while the inner drops were formed in the dripping mode. At $Ca_2 < 0.7 \times 10^{-4}$, a thin oil shell burst during drop formation and the inner phase leaked into the continuous phase. At $Ca_2 > 7.9 \times 10^{-4}$, the jet diameter reached the orifice diameter causing wetting of the orifice and the formation of double emulsion drops failed.

The dripping-to-narrowing-jetting transition could not occur by changing Q_2 at constant Ca_3 and Ca_1. However, the widening-to-narrowing jetting transition, which was not reported earlier, was achieved by gradually increasing Ca_3 at relatively high inner phase flow rate.

Fig. 6 shows the transition from widening to narrowing jetting achieved by increasing Ca_3 at constant Ca_1 and Ca_2, starting from a Ca_1 value which was 13 times larger than in Fig. 5. At low Ca_3 (Fig. 6a and b), both inner and outer drops were formed in the widening jetting mode ($\log\zeta$ = 5.4–5.5). The drops were large and the jets occupied a significant portion of the tube cross section. At high Ca_3 (Fig. 6e and f), both inner and outer drops were formed in the narrowing jetting mode ($\log\zeta$ = 4.7–4.8). For intermediate Ca_3 values (Fig. 6c–d), the regime was not clearly defined and $\log\zeta$ was close to the critical value of 5.0 at which the transition from widening to narrowing jetting occurs ($\log\zeta$= 4.9–5.2). In Fig. 6c, monodisperse core-shell drops with thin shells were formed at relatively high flow rates of the inner and outer phases.

By increasing Ca_3 from 4.6×10^{-3} to 9.2×10^{-3}, the length of the jet decreased due to increasing shear exerted by the outer fluid, causing a faster jet pinch-off and formation of smaller drops.

At the transition between the widening and narrowing jetting ($\log\zeta \approx 5$, Fig. 6d), the inner drops reached the minimum size and the neck of the middle phase between the first and second inner drop was stable, causing the formation of dual-core double-emulsion drops with tightly packed core drops. Interestingly, two core drops were also formed at the transition between dripping and widening jetting (Fig. 5e), but the outer drops were much larger. Finally, the increase in Ca_3 from 15.3×10^{-3} to 21.5×10^{-3} (Fig. 6d–f) resulted in shear-driven stretching of the inner phase to an increasingly long and narrow jet, which led to small drops.

3.5. Effect of distance between inner capillaries on drop generation

Fig. 7 shows the effect of distance between the two orifices, ΔL, on the drop formation behaviour at constant fluid flow rates. Without interrupting the drop generation process, the injection capillary was gradually moved in the downstream direction. The inner phase was 5 wt% aqueous solution of glycerol, the middle phase was 2 wt% DC 749 in PDMS fluid, and the continuous aqueous phase contained 40 wt% glycerol and 2 wt% PVA.

At $\Delta L/D_{orif} = -1$, due to low shear from the surrounding middle phase, the inner drops grew to a large size before detachment from

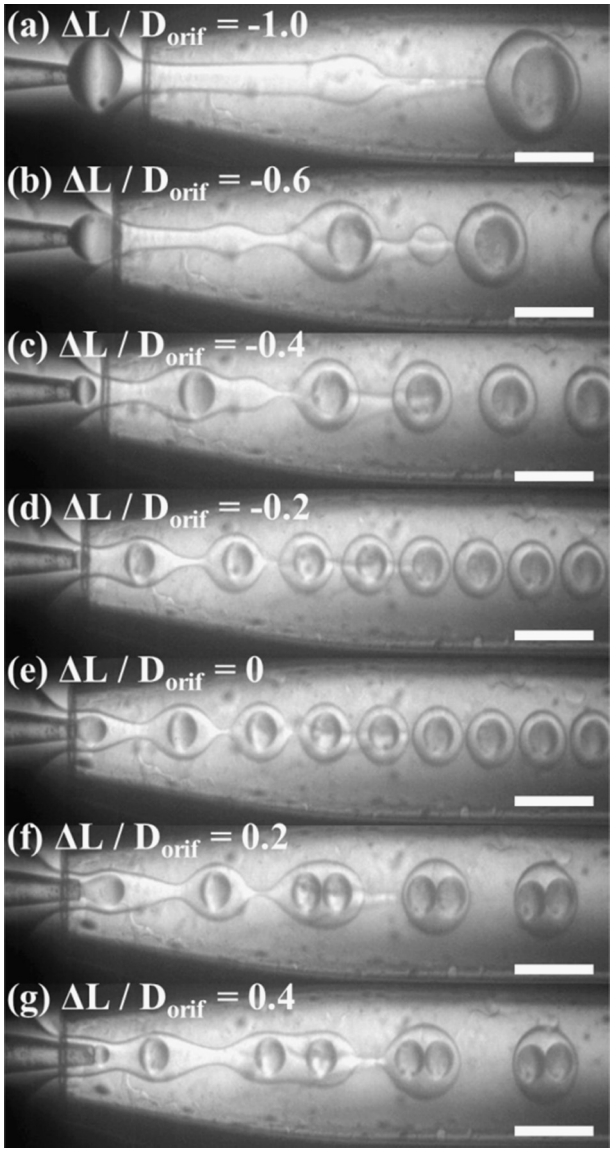

Fig. 7. The effect of distance between the two inner capillaries, ΔL, on the generation of double emulsion drops. Q_1 = 2 mL/h, Q_2 = 7 mL/h, Q_3 = 35 mL/h, ρ_1 = 1012 kg/m^3, ρ_2 = 940 kg/m^3, ρ_3 = 1107 kg/m^3, μ_1 = 1.2 mPa s, μ_2 = 10.4 mPa s, μ_3 = 7.9 mPa s, σ_{12} = 29.9 mN/m, σ_{23} = 31.8 mN/m, D_{orif} = 376 μm, and D_N = 50 μm. All the scale bars are 400 μm.

the tip of the injection tube. An increase in $\Delta L/D_{orif}$ from −1 to −0.2 caused a 2.3-fold reduction in D_1 from 406 to 179 μm. By approaching the orifice of the collection tube, the growing inner drops experienced an increasing shear from the middle fluid pulling the inner jet through the orifice at higher force. Therefore, increased shear accelerated the pinch-off of inner drops causing a reduction in D_1. At $\Delta L = 0$, the double emulsion drops reached the minimum size, because the jet experienced the highest shear. At $\Delta L > 0$, due to increasing cross-sectional area of the collection tube, the shear exerted by the continuous phase was smaller, causing jetting of the middle phase and formation of outer drops with two inner drops [34,43]. However, both inner and outer drops were highly uniform.

The formation and advection of inner drops can considerably destabilise the outer interface and suppress the middle phase jetting. At $\Delta L/D_{orif} = -1$, when the inner drops were formed relatively far from the outer interface, the middle phase jet was very stable. Therefore, a long middle phase jet was developed

within the collection tube, which eventually broke up into large drops. When the inner drops were formed very close to the orifice, e.g., at $\Delta L/D_{orif} = -0.2$, the growing inner drops strongly interacted with the outer interface. In this geometry, the outer interface was significantly deformed by the inner drops, which led to hydrodynamic instabilities in the jet and caused its early break-up into smaller drops. At $\Delta L/D_{orif} = 0.2$ or 0.4, a very thin stream of the middle phase was formed at the entrance of the collection tube, due to the relatively long distance between the drop generation and the entry section of the tube. Further thinning of the middle phase stream around the injection tube at $\Delta L/D_{orif} > 0.4$ caused interruption of the middle phase flow and double emulsion drops failed to form.

4. Conclusions

The developed Volume of Fluid-Continuum Surface Force (VOF-CSF) numerical model was successfully validated with existing analytical solutions [21,28]. The velocity profile at the entry section of the tube was flat in dripping and widening jetting mode, while a saddle-shaped profile was observed in narrowing jetting mode. The numerical results were used to develop a dimensionless parameter, ζ, for prediction of drop formation mode, which is a function of the capillary numbers of the three fluids and the device geometry. For $\log\zeta > 5.7$, double emulsion drops were formed in dripping mode, the widening jetting was observed for $5 < \log\zeta < 5.7$, while the narrowing jetting occurred at $\log\zeta < 5$. The dimensionless criterion ζ was correlated with the ratio of the break-up length to drop diameter and tested against a large number of numerical and experimental results to show its high accuracy in predicting the drop formation mode.

Narrowing jetting reported in numerical simulation studies [29,35] was achieved starting from widening jetting by increasing the flow rate of the outer fluid at constant flow rates of the inner and middle phases. Near the transition between widening jetting and narrowing jetting, it was possible to generate monodispersed core-shell drops with thin shells at much higher flow rates of inner fluid than in the dripping mode.

A glue-free reusable capillary device was used to change the separation distance between the capillary inlets during operation to manipulate the drop formation behaviour. The device consists of two coaxial round capillaries, and therefore, has a true axisymmetric geometry, which differs from the quasi-axisymmetric geometry of a recently fabricated reusable capillary device [44]. The size of core-shell drops was significantly affected by changing the distance between the two tapered capillaries. The minimum drop size was achieved when the orifice of the injection tube was placed exactly at the entry section of the collection tube. In future work, the capillary device will be equipped with a thermoelectric generator in order to study the effect of temperature on generation of double emulsion drops.

Acknowledgements

The authors gratefully acknowledge the financial support for this work received from the EPSRC – United Kingdom grant EP/HO29923/1. The authors also thank Dr Andrew S. Utada, Prof André R. Studart, and Dr Wei Chen for their helpful discussions on validation of the numerical model.

Appendix A. Supplementary material

Supplementary data associated with this article can be found, in the online version, at http://dx.doi.org/10.1016/j.jcis.2017.05.115.

References

[1] M.H. Lee, K.C. Hribar, T. Brugarolas, N.P. Kamat, J.A. Burdick, D. Lee, Harnessing interfacial phenomena to program the release properties of hollow microcapsules, Adv. Funct. Mater. 22 (2012) 131–138, http://dx.doi.org/10.1002/adfm.201101303.
[2] A. Abbaspourrad, S.S. Datta, D.A. Weitz, Controlling release from pH-responsive microcapsules, Langmuir 29 (2013) 12697–12702, http://dx.doi.org/10.1021/la403064f.
[3] B. Kim, T.Y. Lee, A. Abbaspourrad, S.H. Kim, Perforated microcapsules with selective permeability created by confined phase separation of polymer blends, Chem. Mater. 26 (2014) 7166–7171, http://dx.doi.org/10.1021/cm503831t.
[4] N. Vilanova, C. Rodríguez-Abreu, A. Fernández-Nieves, C. Solans, Fabrication of novel silicone capsules with tunable mechanical properties by microfluidic techniques, ACS Appl. Mater. Interfaces. 5 (2013) 5247–5252, http://dx.doi.org/10.1021/am4010896.
[5] H. Lee, C.H. Choi, A. Abbaspourrad, C. Wesner, M. Caggioni, T. Zhu, et al., Encapsulation and enhanced retention of fragrance in polymer microcapsules, ACS Appl. Mater. Interfaces. 8 (2016) 4007–4013, http://dx.doi.org/10.1021/acsami.5b11351.
[6] F. Li, X. Wang, D. Wu, Fabrication of multifunctional microcapsules containing n-eicosane core and zinc oxide shell for low-temperature energy storage, photocatalysis, and antibiosis, Energy Convers. Manage. 106 (2015) 873–885, http://dx.doi.org/10.1016/j.enconman.2015.10.026.
[7] J.J. Vericella, S.E. Baker, J.K. Stolaroff, E.B. Duoss, J.O. Hardin, J. Lewicki, et al., Encapsulated liquid sorbents for carbon dioxide capture, Nat. Commun. 6 (2015) 6124–6130, http://dx.doi.org/10.1038/ncomms7124.
[8] S.A. Nabavi, G.T. Vladisavljević, S. Gu, V. Manović, Semipermeable elastic microcapsules for gas capture and sensing, Langmuir 32 (2016) 9826–9835, http://dx.doi.org/10.1021/acs.langmuir.6b02420.
[9] K. Nakagawa, S. Iwamoto, M. Nakajima, A. Shono, K. Satoh, Microchannel emulsification using gelatin and surfactant-free coacervate microencapsulation, J. Colloid Interface Sci. 278 (2004) 198–205, http://dx.doi.org/10.1016/j.jcis.2004.05.031.
[10] J.H. Han, B.M. Koo, J.W. Kim, K.D. Suh, A facile approach to synthesize uniform hydrogel shells with controllable loading and releasing properties, Chem. Commun. (Camb). (2008) 984–986, http://dx.doi.org/10.1039/b715557c.
[11] E. Donath, G.B. Sukhorukov, F. Caruso, S.A. Davis, H. Möhwald, Novel hollow polymer shells by colloid-templated assembly of polyelectrolytes, Angew. Chemie, Int. Ed. 37 (1998) 2201–2205. doi:10.1002/(SICI)1521-3773(19980904)37:16<2201::AID-ANIE2201>3.0.CO;2-E..
[12] P.J. Dowding, R. Atkin, B. Vincent, P. Bouillot, Oil core – polymer shell microcapsules prepared by internal phase separation from emulsion droplets. I. Characterization and release rates for microcapsules with polystyrene shells, (2004) 11374–11379. doi: 10.1021/la048561h.
[13] E. Mathiowitz, H. Bernstein, S. Giannos, P. Dor, T. Turek, R. Langer, Polyanhydride microspheres. IV. Morphology and characterization of systems made by spray drying, J. Appl. Polym. Sci. 45 (1992) 125–134, http://dx.doi.org/10.1002/app.1992.070450115.
[14] T. Nisisako, T. Hatsuzawa, Microfluidic fabrication of oil-filled polymeric microcapsules with independently controllable size and shell thickness via Janus to core-shell evolution of biphasic droplets, Sens. Actuat. B Chem. 223 (2016) 209–216, http://dx.doi.org/10.1016/j.snb.2015.09.085.
[15] N. Pannacci, H. Bruus, D. Bartolo, I. Etchart, T. Lockhart, Y. Hennequin, et al., Equilibrium and nonequilibrium states in microfluidic double emulsions, Phys. Rev. Lett. 101 (2008) 164502–164505, http://dx.doi.org/10.1103/PhysRevLett.101.164502.
[16] A.R. Abate, J. Thiele, D.A. Weitz, One-step formation of multiple emulsions in microfluidics, Lab Chip 11 (2011) 253–258, http://dx.doi.org/10.1039/c0lc00236d.
[17] T. Nisisako, S. Okushima, T. Torii, Controlled formulation of monodisperse double emulsions in a multiple-phase microfluidic system, Soft. Matter 1 (2005) 23–27, http://dx.doi.org/10.1039/b501972a.
[18] G. Nurumbetov, N. Ballard, S.A.F. Bon, A simple microfluidic device for fabrication of double emulsion droplets and polymer microcapsules, Polym. Chem. 3 (2012) 1043–1047, http://dx.doi.org/10.1039/C2PY00605G.
[19] Z. Chang, C.A. Serra, M. Bouquey, L. Prat, G. Hadziioannou, Co-axial capillaries microfluidic device for synthesizing size- and morphology-controlled polymer core-polymer shell particles, Lab Chip 9 (2009) 3007–3011, http://dx.doi.org/10.1039/b913703c.
[20] L.Y. Chu, A.S. Utada, R.K. Shah, J.W. Kim, D.A. Weitz, Controllable monodisperse multiple emulsions, Angew. Chemie, Int. Ed. 46 (2007) 8970–8974, http://dx.doi.org/10.1002/anie.200701358.
[21] A.S. Utada, E. Lorenceau, D.R. Link, P.D. Kaplan, H.A. Stone, D.A. Weitz, Monodisperse double emulsions generated from a microcapillary device, Science 308 (2005) 537–541, http://dx.doi.org/10.1126/science.1109164.
[22] G.T. Vladisavljević, H. Shahmohamadi, D.B. Das, E.E. Ekanem, Z. Tauanov, L. Sharma, Glass capillary microfluidics for production of monodispersed poly (dl-lactic acid) and polycaprolactone microparticles: experiments and numerical simulations, J. Colloid Interface Sci. 418 (2014) 163–170, http://dx.doi.org/10.1016/j.jcis.2013.12.002.
[23] A.S. Utada, A. Fernandez-Nieves, J.M. Gordillo, D.A. Weitz, Absolute instability of a liquid jet in a coflowing stream, Phys. Rev. Lett. 100 (2008) 1–4, http://dx.doi.org/10.1103/PhysRevLett.100.014502.

[24] C. Duprat, C. Ruyer-Quil, S. Kalliadasis, F. Giorgiutti-Dauphiné, Absolute and convective instabilities of a viscous film flowing down a vertical fiber, Phys. Rev. Lett. 98 (2007) 48–51, http://dx.doi.org/10.1103/PhysRevLett. 98.244502.
[25] T.P. Lagus, J.F. Edd, A review of the theory, methods and recent applications of high-throughput single-cell droplet microfluidics, J. Phys. D Appl. Phys. 46 (2013) 114005–114025, http://dx.doi.org/10.1088/0022-3727/46/11/114005.
[26] L. Shui, S. Pennathur, J.C.T. Eijkel, A. van den Berg, Multiphase flow in lab on chip devices: a real tool for the future?, Lab Chip 8 (2008) 1010–1014, http://dxdoi.org/10.1039/b808974b.
[27] A.S. Utada, L.Y. Chu, A. Fernandez-Nieves, D.R. Link, C. Holtze, D.A. Weitz, Dripping, jetting, drops, and wetting: the magic of microfluidics, MRS Bull. 32 (2007) 702–708, http://dx.doi.org/10.1557/mrs2007.145.
[28] R.M. Erb, D. Obrist, P.W. Chen, J. Studer, A.R. Studart, Predicting sizes of droplets made by microfluidic flow-induced dripping, Soft Matter 7 (2011) 8757–8761, http://dx.doi.org/10.1039/c1sm06231j.
[29] S.A. Nabavi, G.T. Vladisavljević, S. Gu, E.E. Ekanem, Double emulsion production in glass capillary microfluidic device: parametric investigation of droplet generation behaviour, Chem. Eng. Sci. 130 (2015) 183–196, http://dx.doi.org/10.1016/j.ces.2015.03.004.
[30] A.S. Utada, A. Fernandez-Nieves, H.A. Stone, D.A. Weitz, Dripping to jetting transitions in coflowing liquid streams, Phys. Rev. Lett. 94502 (2007) 1–4, http://dx.doi.org/10.1103/PhysRevLett.99.094502.
[31] E. Castro-Hernández, V. Gundabala, A. Fernández-Nieves, J.M. Gordillo, Scaling the drop size in coflow experiments, New J. Phys. 11 (2009) 075021–075037, http://dx.doi.org/10.1088/1367-2630/11/7/075021.
[32] G.F. Christopher, S.L. Anna, Microfluidic methods for generating continuous droplet streams, J. Phys. D Appl. Phys. 40 (2007) 319–336, http://dx.doi.org/10.1088/0022-3727/40/19/R01.
[33] Y. Chen, L. Wu, C. Zhang, Emulsion droplet formation in coflowing liquid streams, Phys. Rev. E 87 (2013) 013002, http://dx.doi.org/10.1103/PhysRevE.87.013002.
[34] D. Lee, D.A. Weitz, Nonspherical colloidosomes with multiple compartments from double emulsions, Small 5 (2009) 1932–1935, http://dx.doi.org/10.1002/smll.200900357.
[35] Y. Chen, L. Wu, L. Zhang, Dynamic behaviors of double emulsion formation in a flow-focusing device, Int. J. Heat Mass Transf. 82 (2015) 42–50, http://dx.doi.org/10.1016/j.ijheatmasstransfer.2014.11.027.
[36] C.W. Hirt, B.D. Nichols, Volume of fluid (VOF) method for the dynamics of free boundaries, J. Comput. Phys. 39 (1981) 201–225, http://dx.doi.org/10.1016/0021-9991(81)90145-5.
[37] J.U. Brackbill, D.B. Kothe, C. Zemach, A continuum method for modeling surface tension, J. Comput. Phys. 100 (1992) 335–354, http://dx.doi.org/10.1016/0021-9991(92)90240-Y.
[38] S.A. Nabavi, S. Gu, G.T. Vladisavljevi, E.E. Ekanem, Dynamics of double emulsion break-up in three phase glass capillary microfluidic devices, J. Colloid Interface Sci. 450 (2015) 279–287, http://dx.doi.org/10.1016/j.jcis.2015.03.032.
[39] C. Martino, S. Berger, R.C.R. Wootton, A.J. deMello, A 3D-printed microcapillary assembly for facile double emulsion generation, Lab Chip 14 (2014) 4178–4182, http://dx.doi.org/10.1039/C4LC00992D.
[40] S. Tomotika, On the instability of a cylindrical thread of a viscous liquid surrounded by another viscous fluid, Proc. R. Soc. London A Math. Phys Eng. Sci. 150 (1935) 322–337, http://dx.doi.org/10.1098/rspa.1935.0104.
[41] S. Tomotika, Breaking up of a drop of viscous liquid immersed in another viscous fluid which is extending at a uniform rate, Proc. R. Soc. London A Math. Phys Eng. Sci. 153 (1936) 302–318, http://dx.doi.org/10.1098/rspa.1936.0003.
[42] T.R. Powers, D. Zhang, R.E. Goldstein, H.A. Stone, Propagation of a topological transition: the Rayleigh instability, Phys. Fluids 10 (1998) 1052–1057, http://dx.doi.org/10.1063/1.869650.
[43] S.A. Nabavi, G.T. Vladisavljević, V. Manović, Mechanisms and control of single-step microfluidic generation of multi-core double emulsion droplets, Chem. Eng. J. 322 (2017) 140–148, http://dx.doi.org/10.1016/j.cej.2017.04.008.
[44] B.R. Benson, H.A. Stone, R.K. Prud'homme, An "off-the-shelf" capillary microfluidic device that enables tuning of the droplet breakup regime at constant flow rates, Lab Chip 7 (2013) 4507–4511, http://dx.doi.org/10.1039/c3lc50804h.